Superior photocatalytic disinfection effect of Ag-3D ordered mesoporous CeO$_2$ under visible light

Qixing Zhou[*], Shuanglong Ma, Sihui Zhan

Key Laboratory of Pollution Processes and Environmental Criteria (Ministry of Education)/Tianjin Key Laboratory of Environmental Remediation and Pollution Control, College of Environmental Science and Engineering, Nankai University, Tianjin 300350, China

ARTICLE INFO

ABSTRACT

Ordered mesoporous Ag/CeO$_2$ nanocomposites were prepared by combining nanocasting with photo-assisted reduction. The heterogeneous photoreactivity of the prepared samples was tested for inactivating *Escherichia coli* (*E. coli*). These mesoporous Ag/CeO$_2$ nanocomposites exhibited superior photocatalytic disinfection efficiency than mesoporous CeO$_2$ and bulk CeO$_2$, respectively. Doping Ag species could extend the absorption range to visible light area and enhance the concentration of Ce^{3+} ions and oxygen vacancies, which had significant influence on the surface properties of CeO$_2$. Moreover, it is the first time to verify that created midgap states through doping Ag can significantly lower the threshold of incident photon energy and broaden the adsorption spectrum demonstrated by experimental studies and density functional theory (DFT) calculations. The enhanced disinfection mechanism was attributed to the fact that the novel mesoporous structure can promote the mass transfer process and the interfacial interaction between Ag species and CeO$_2$ and lead to reduced recombination of free charges, rapid separation and transportation of photogenerated electrons-holes. This work provides a new method to develop novel mesoporous plasmonic photocatlysts for disinfection using solar radiation.

1. Introduction

Drinking water disinfection against pathogenic bacteria is an important treatment process for protecting public health [1]. At present, more than one billion people in the world do not have access to safe drinking water [2,3]. As a result, waterborne diseases such as cholera, typhoid, and diarrhea are very common in developing countries [4,5], where critical infrastructures are lacking to implement existing disinfection methods such as UV irradiation, chlorination, and ozonation [6]. Photocatalytic disinfection has been considered as one of the most sustainable and cost-effective disinfection processes since the photon-based platinum-doped TiO$_2$ mediated photocatalysis was first reported in 1985 [7–10]. In contrast to other water purification technology, such as chlorination and ozonation, the photocatalytic disinfection seems to be much preferable because of much less created disinfection by-products, convenient and environmental operation process, and usage of abundant solar energy [11].

As the one of the most abundant rare earth oxides, CeO$_2$ is attractive for its excellent physical and chemical properties. It has been exploited with numerous technological applications in a lot of fields, such as electrochemical cells [12,13], optical devices [14], biomaterials [15], and photocatalysts [16–19]. As an *n*-type semiconductor, fluorite CeO$_2$

showed widely application for pollutants elimination with attractive features such as low-cost, chemical inertness, photo-stability and non-toxicity [20,21]. Among the different properties of CeO$_2$, the transformation between Ce^{4+} and Ce^{3+} by oxidation-reduction cycles is possibly the most important one, because which produces oxygen vacancies in their structure [22,23]. Generally, catalysts with different morphologies or structures exhibit very different physical and chemical properties [24]. CeO$_2$ with different morphologies such as rods [25], tubes [26], spheres [27] and sheets [28], have been synthesized and obtained a large number applications in catalytic fields. Recently, considerable attentions have been paid to the developing mesoporous materials on account of their large specific surface area, interconnected channels and ordered mesoporous structure as well as their controllable pore diameters and volumes [29,30]. Among these mesoporous materials, highly ordered mesoporous CeO$_2$ and its modified nanocomposites have been extensively studied for CO oxidation [31], purification of volatile organic compounds [32], reverse water gas shift reaction [33].

The CeO$_2$ plasmonic photocatalysts doped with noble metal including silver, gold, and platinum, are attracting more and more interests due to their significant photocatalytic activity [34–36]. Generally, noble metal nanoparticles such as Ag species are used as dopants

---

to improve the photocatalytic effect because they have lower Fermi energy levels compared to most semiconductor photocatalysts, and thus a Schottky barrier can be formed when they form an intimate contact, which can prevent the recombination of free charge carriers [37]. The plasmonic photocatalysts exhibited obvious advantages because they combine the optoelectronic properties of semiconductor with the surface plasmon resonance (SPR) effect and excellent conductivity of noble metal nanoparticles [38]. The SPR effect could increase its light absorption activity by scattering resonant photons and therefore lead to longer optical path lengths. In addition, the heterogeneous interface between noble metal and semiconductor could accelerate to the separation of charge carriers and prolong the life-time of photoinduced electron-hole pairs [39]. It has also been reported that plasmonic nanometal can provide driving forces to catalytic reactions by generating hot electrons and the photothermal effect [40].

In this work, highly ordered mesoporous Ag doped CeO_2 photocatalysts with different Ag doping amounts were synthesized by a nanocasting route and photo-assisted reduction methods. The catalysts were used as biocides against *E. coli* under visible light. In contrast to bulk and mesoporous CeO_2, the Ag/CeO_2 presented considerably increased disinfection activity with the optimal Ag amounts of 2 wt%. The promotion mechanisms were systematically characterized by TEM, Raman spectra, BET, XPS and photo-electrochemical methods. It can be found that the loading of Ag species facilitated the formation of oxygen vacancy, enhanced the absorption of visible light, and reduced the recombination of photogenerated electron and hole, which was favorable for the catalytic reaction. Furthermore, the density functional theory (DFT) calculations indicated that the midgap states were created after doping Ag which significantly lower the threshold of incident photon energy and broaden the adsorption spectrum and thereby promoted the disinfection activity.

2. Experimental

2.1. Materials

All chemicals used in this work are analytical grade. All chemicals were used as-received without any further purification. Pluronic P123, tetraethyl orthosilicate (TEOS) and cerium nitrate hexahydrate (Ce(NO_3)$_2$·6H_2O) were purchased from Aladdin Corporation (Shanghai, China). Hydrochloric acid (HCl), anhydrous ethanol (C_2H_5OH), *n*-butanol, sodium hydroxide (NaOH) and silver nitrate ($AgNO_3$) were purchased from Jiangtian Chemical Technology Co. Ltd. (Tianjin, China).

2.2. Photocatalyst preparation

In order to synthesize the ordered mesoporous CeO_2, mesoporous KIT-6 silica was used as a hard template which was prepared according to the method by Soni et al. [41]. Typically, 1.8 g of Ce(NO_3)$_2$·6H_2O were dissolved in 30 mL anhydrous ethanol, and then 1.0 g of KIT-6 was added to the above mixture. After the mixture was stirred overnight at room temperature, the above sample was dried at 80 °C for 6 h and then sintered at 500 °C at a rate of 1 °C/min from room temperature for 4 h in a muffle furnace. After cooling to room temperature, the obtained powders were washed with 2 M NaOH aqueous solutions for three times to remove the silica template, followed by washing with deionized water several times until neutral and then dried at 60 °C for 24 h in an oven. The bulk CeO_2 (CeO_2-B) was prepared as the above method without the addition of KIT-6.

The Ag/CeO_2 mesoporous nanocomposites were prepared by $AgNO_3$ impregnation and photo-assisted reduction method. 1.0 g of as-prepared mesoporous CeO_2 (CeO_2-M) sample was ultrasonically dispersed in 75 mL of deionized water for 30 min. Then, 10 mL of $AgNO_3$ aqueous solution with different concentrations (1.57, 3.15, 4.72 mg/mL) was dropwise added to the above CeO_2 solution, in which Ag contents were 1, 2, and 3 wt%, respectively. The mixture was stirred for 1 h to reach

adsorption balance followed by being stirred for 2 h under the irradiation of a 300 W Xenon arc lamp (CEL-HXF300, Ceaulight, Beijing, China). The resultant suspension was centrifuged and washed with deionized water for three times to remove the residual Ag^+. Finally, the product was dried in an oven at 60 °C for 24 h. The mesoporous composites were denoted as Ag(*X*)/CeO_2-M. *X* represents Ag/CeO_2-M mass ratio in preparation, which were 1, 2, and 3%, respectively.

2.3. Characterizations

The morphology observation of samples was carried out by a transmission electron microscopy (TEM, JEOL Model JEM-1200EX). The X-ray diffraction (XRD) patterns of samples were conducted via an X-ray diffractometer (Rigaku D/Max 2500PC) with a CuKα radiation. Raman spectra were obtained with Raman Microscope (Renishaw inVia, Renishaw). Light absorption (reflectance) spectra were recorded by UV-vis-NIR diffuse reflectance spectrum (Shimadzu Corporation, UV-3600, Japan). X-ray photo-electron spectroscopy (XPS) spectra were collected on an ESCALAB250 multi-technique X-ray photoelectron spectrometer using a monochromatic Al Kα X-ray source. N_2 adsorption-desorption data were obtained using a Quantachrom SI Micromeritics apparatus, and the isotherms were evaluated with the Barrett-Joyner-Halenda (BJH) theory. The visible light irradiation was obtained from a 300 W Xenon arc lamp (CEL-HXF300, Ceaulight, Beijing). The room-temperature photoluminescence (PL) spectra of samples were investigated using an Edinburgh Instruments FLS920P equipped with a Xe lamp-920 with an excitation wavelength of 374 nm. The Superoxide dismutase (SOD) activities were determined using a SOD assay kit (A001-1, Nanjing JianCheng Bioengineering Institute, China). The Catalase (CAT) activities were determined using a CAT assay kit (A007-1, Nanjing JianCheng Bioengineering Institute, China). ESR signals of reactive species trapped by 5, 5-diemthyl-1-pyrroline N-oxide (DMPO) were detected using a Magnet Tech MS400 spectrometer. The photoelectrochemical performance was measured in a three electrode quartz cells system including a saturated calomel electrode (SCE) as reference electrode, platinum plate as counter electrode, and ITO glass coated with CeO_2-M and Ag(2%)/CeO_2-M as the working electrode with 0.1 M Na_2SO_4 as electrolyte. The photoelectrochemical experiment results were recorded by an electrochemical station (CHI660D, Shanghai Chenhua, China). The photocurrent responses of the prepared samples with visible light on and off were measured at 0.0 V. Electrochemical impedance spectra (EIS) were measured at 0.0 V over the frequency range of 0.05–10^3 Hz with an AC voltage of 5 mV. In order to calculate the flat-band potentials, Mott-Schottky plots were performed at a frequency of 1000 Hz with 10 mV amplitude in the dark. All the potential were measured relative to the SCE reference electrode and converted to vs reversible hydrogen electrode (RHE) scale according to the following equation:

$$E_{vs.RHE} = E_{vs.SCE} + E_{SCEvs.NHE} + 0.059 \times pH \qquad (1)$$

Where $E_{vs.RHE}$ is the calculated potential vs RHE, $E_{vs.SCE}$ is the measured potential, pH is approximately 7.0 and $E_{SCEvs.NHE}$ is approximately 0.2415 V at room temperature.

2.4. Disinfection performance

The photocatalytic inactivation of *E. coli* (Gram-negative) was carried out by a 300 W Xenon arc lamp (CEL-HXF300, Ceaulight, Beijing) with a UV cutoff (λ < 420 nm) as a light source. The bacteria were grown in nutrient broth at 37 °C for 15 h to yield a cell count of approximately 10^9 colony forming units (cfu)/mL. Then bacterial bodies were collected by centrifugation (5000*g* for 10 min) and washed using sterile 0.85% (wt/vol) saline solution for three times. The final cell density was adjusted to about 10^7 cfu/mL using 0.85% (wt/vol) saline solution for disinfection experiment. 250 μL of photocatalyst saline

solution (4 mg/mL) was added to 10 mL of bacteria solution (10^7 cfu/mL) in a 50 mL beaker. The above solution was mixed using a magnetic stirrer at room temperature under the visible light. During the disinfection process, the mixture was retrieved at a planned time interval and the bacteria density was calculated by the standard plate count method. During the process, the plates were incubated at 37 °C for 24 h. The number of colonies was counted through visual inspection. For revealing the influence of humic acid, the experimental method was also same as the above process except that 50 μL of humic acid sterile solution with different concentrations (50, 100, 200, 400 mg/L) was added, leading to 0.25, 0.5, 1, and 2 mg/L of humic acid in the final reaction system. All the experiments were repeated for three times.

2.5. Fluorescent-based cell live/dead test

The bacteria live/dead test was further confirmed by fluorescent-based test. The mixture of bacteria suspension (10^9 cfu/mL) and Ag(2%)/CeO$_2$-M (100 μg/mL) were mixed by a magnetic stirrer at room temperature under the visible light. The mixture was withdrawn at 0, 30, 60, 90, and 120 min, respectively. Then the mixture were stained with SYTO9 and PI (propidium iodide) (LIVE/DEAD Baclight Bacterial Viability kit) according to the direction, and pictured using a laser scanning fluorescence microscopy (Olympus, FV1000).

2.6. SEM and AFM observation of E. coli

The morphology of *E. coli* was imaged by scanning electron microscopy (Hitachi S-4800, Japan) and AFM (Agilent 5420 AFM instrument, CA). The bacteria at different irradiation time (0, 30, 60, 90, and 120 min) were fixed on silicon pellet for SEM and mica sheet for AFM with 2.5% glutaraldehyde solution in 4 °C overnight. Then the samples were sequentially dehydrated with 30, 50, 70, 90, and 100% ethanol for 20 min, respectively. The samples were lyophilized, gold sputter-coated before SEM analysis.

3. Results and discussion

3.1. Characterizations of photocatalysts

The disordered morphologies of CeO$_2$-B were exhibited in Fig. 1a and b, which indicated the irregular arrangement of small CeO$_2$ crystals resulting into a few inhomogeneous pores. As shown in Fig. 1c and d,

the CeO$_2$-M displayed well-arranged morphology and highly ordered mesoporous structure, indicating that ordered mesoporous CeO$_2$ was replicated successfully by thermal decomposition of metal precursors within the restricted channels of KIT-6. The high resolution TEM images in Fig. 1e and f showed the well-ordered cubic array of mesopores with a diameter about 3 nm, and the pore walls were composed of individual hexagonal CeO$_2$ nanocrystals with a diameter about 6 nm. The lattice fringes of CeO$_2$ attributed to the (111) crystallographic planes (d = 0.31 nm) and the (100) crystallographic planes (d = 0.28 nm) can be clearly observed [42,43]. After the photo-deposition of Ag species, there is no obvious difference between the morphology of Ag(2%)/CeO$_2$-M (Fig. 2a) and pure CeO$_2$-M and the highly ordered 3D mesoporous structure was still maintained. The Ag nanoparticles were not observed on the surface of CeO$_2$, which can be attributed to the low loading amount of Ag and the formation of too small Ag nanoparticles. According to the ICP (IRIS Intrepid II XSP, Thermo Elemental) results, the mass percent of Ag in Ag(1%)/CeO$_2$-M, Ag(2%)/CeO$_2$-M, and Ag(3%)/CeO$_2$-M is 0.68%, 1.50%, and 2.19%, respectively. On the other hand, because of its highly ordered mesoporous and interconnected channels, many Ag ions were absorbed in the pores of CeO$_2$-M during the mixture of CeO$_2$-M and AgNO$_3$, and thus Ag nanoparticles were deposited in the pores of CeO$_2$-M instead of on its surface. Furthermore, the energy-dispersive X-ray spectroscopy (EDS) elemental mapping for Ce, O, and Ag was carried out to observe the elements distribution in Ag(2%)/CeO$_2$-M (Fig. 2b–e). It can be found that the Ce, O, and Ag were uniformly distributed, which confirmed the successful synthesis of Ag(2%)/CeO$_2$-M composite photocatalyst.

The SEM images of CeO$_2$-B, CeO$_2$-M, and Ag(2%)/CeO$_2$-M were taken to provide a whole understanding of their morphologies. As shown in Fig. S1a–c, the CeO$_2$-B samples showed shapes of irregular blocks without ordered mesoporous structure. From the low resolution SEM images of CeO$_2$-M (Fig. S1d and e) and Ag(2%)/CeO$_2$-M (Fig. S1 g and h), both the samples exhibited spherical morphologies. As the high resolution SEM image of CeO$_2$-M and Ag(2%)/CeO$_2$-M in Fig. S1f and i, the well-ordered mesoporous structure of KIT-6 was retained, which was conducive to the transport of reactants and reactive species and further accelerated the photocatalytic reaction.

The wide-angle XRD patterns of as-prepared samples were displayed in Fig. 3a. The sphere represented the characteristic peaks of CeO$_2$. For all samples, the eight distinct diffraction peaks at 28.6°, 33.1°, 47.5°, 56.3°, 59.1°, 69.4°, 76.7°, and 79.1° were related to the fluorite structure of CeO$_2$ ((JCPDS 34-0394) and could be assigned as (111), (200),
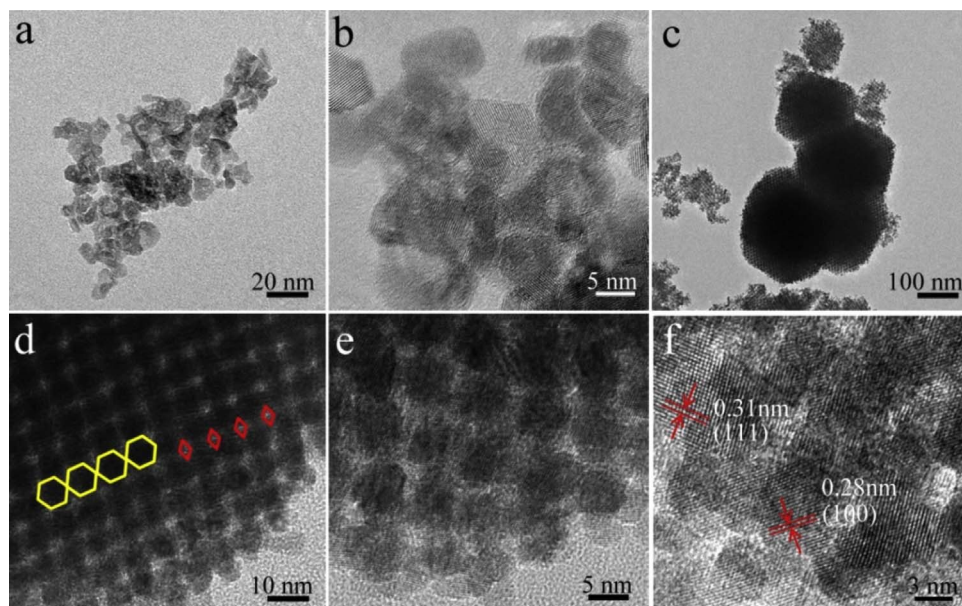

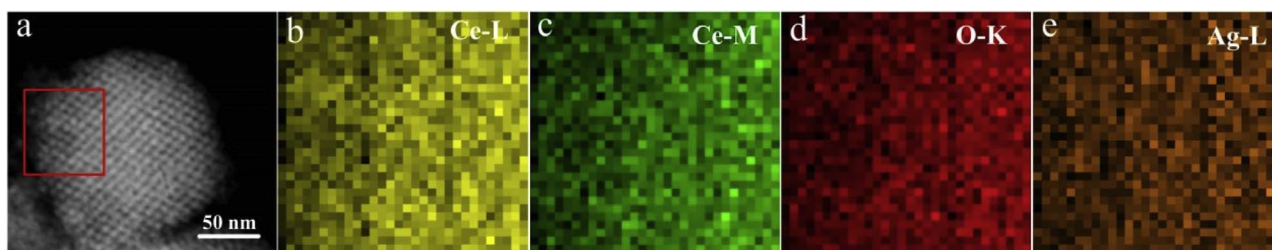**Fig. 1.** TEM images of CeO$_2$-B (a, b) and CeO$_2$-M (c-f).

Fig. 2. TEM image of Ag(2%)/CeO$_2$-M (a). The energy-dispersive X-ray spectroscopy (EDS) elemental mapping of Ag(2%)/CeO$_2$-M (b-e).

(220), (311), (222), (400), (331) and (420) crystal planes, respectively [39]. In contrast to pure CeO$_2$, three additional peaks could be found in Ag/CeO$_2$-M pattern which belonged to the crystal Ag. The diffraction peaks appearing at 2θ = 38.1° and 44.3° can be indexed to (111) and (200) plane of Ag face centered cubic (fcc) phase (JCPDS 65-2871) [6]. For the low-angle XRD patterns in Fig. 3b, the characteristic peaks at 2θ of around 1.2° for the obtained mesoporous samples can be clearly observed, corresponding to the (211) diffraction peak of the cubic Ia3d symmetry of mesoporous silica template, suggesting that the CeO$_2$-M and Ag/CeO$_2$-M samples retained the same regular mesostructures as the KIT-6 plates. Furthermore, with Ag doped, the intensity of diffraction peaks became weaker, and the peak positions shifted to the lower angles, which was possibly attributed to that parts of mesoporous channels were blocked by the deposited Ag crystals. The regularity of mesoporous samples was poorer than pure mesoporous CeO$_2$, which could also be verified from the surface area results.

From Fig. 3c, the adsorption-desorption curves of all the samples could be verified as type IV isotherms. The CeO$_2$-B exhibited a hysteresis loop in a relative pressure ranging from 0.7-0.9, which belonged to type H2 and indicated the presence of pores with ink-bottle pores. However, for all the mesoporous samples, the hysteresis loops in the relative pressure ranging from 0.6 to 0.95 were verified to an intermediate between types H3 and H4, reflecting their slitlike mesoporous structure [31]. The surface area of CeO$_2$-B, CeO$_2$-M, Ag(1%)/CeO$_2$-M, Ag(2%)/CeO$_2$-M, and Ag(3%)/CeO$_2$-M was 70.2, 163.3, 139.0, 137.6, and 137.5 m^2/g, respectively. The surface area of CeO$_2$-M was about twice larger than that of CeO$_2$-B, which was attributed to its highly ordered mesoporous and interconnected channels. The surface area of CeO$_2$-M samples decreased slightly after Ag doped, suggesting that

adsorption sites on the surface of TNS may be took up by the formed Ag nanocrystals. According to the BJH pore size distribution (Fig. 3d and Table S1), CeO$_2$-B and CeO$_2$-M had the porous diameters of the maximum distribution at 10.82 and 3.41 nm, respectively, indicating the narrower pore diameter distribution and smaller pore diameter of CeO$_2$-M, which were similar to the pore-size data obtained from TEM images. The total pore volume of CeO$_2$-M (0.461 cc/g) was significantly larger than that of CeO$_2$-B (0.192 cc/g). The pore diameter and volume slightly decreased after Ag doped, which was possibly attributed to the fact that the deposited Ag nanoparticles blocked the pore channel. Generally, the specific surface area of nanomaterial has a positive correlation with the amount of active reaction sites on its surface [9]. Compared with the non-mesoporous structure, the high specific surface areas and ordered mesoporous of Ag/CeO$_2$-M nanocomposites was conducive to the absorption and diffusion of reactants, leading to relatively higher photocatalytic activity [31].

All the samples showed two main Raman adsorption peaks, a strong peak located around 460 cm^{-1} and a weak peak around 596 cm^{-1} (Fig. S2). The strong peak around 460 cm^{-1} could be attributed to F$_{2g}$ vibration of the fluorite-type structure and it was considered as the symmetric stretching mode of oxygen atoms around cerium ions. While the defect-induced (D) mode around 596 cm^{-1} was related to oxygen vacancies due to the presence of Ce^{3+} in the CeO$_2$ lattice. The peaking fitting of the F$_{2g}$ and D modes in the Raman spectra of all samples were conducted to calculate the ratio (I$_D$/I$_{F2g}$), which was linked to the oxygen defect sites of the catalysts [34]. The I$_D$/I$_{F2g}$ value of CeO$_2$-B, CeO$_2$-M, Ag(1%)/CeO$_2$-M, Ag(2%)/CeO$_2$-M, and Ag(3%)/CeO$_2$-M was 0%, 3.29%, 3.96%, 7.02%, and 4.55%, respectively. It can be found that almost no defects site was found in CeO$_2$-B. However, it is obvious that
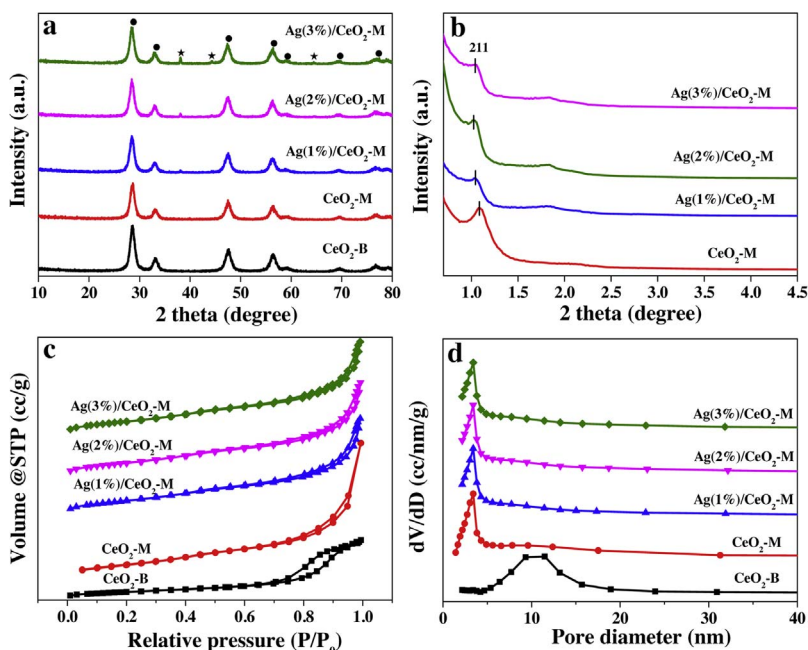
Fig. 3. (a) Wide-angle XRD, (b) low-angle XRD patterns, (c) N$_2$ adsorption-desorption isotherms, and (d) pore diameter distribution.
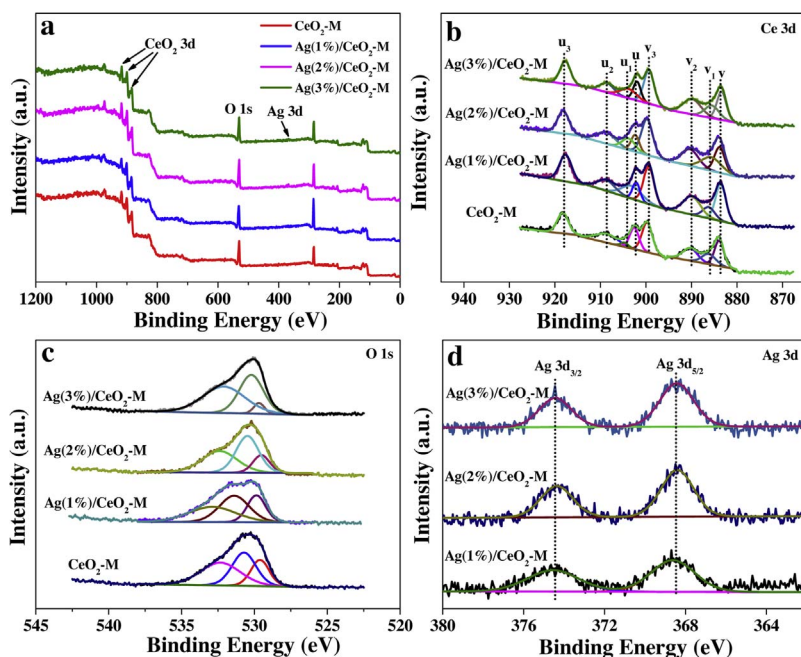
Fig. 4. XPS spectra of CeO$_2$-M, Ag(1%)/CeO$_2$-M, Ag(2%)/CeO$_2$-M, and Ag(3%)/CeO$_2$-M: (a) survey XPS spectrum, (b) Ce 3d, (c) O 1s, and (d) Ag 3d.

there were defects sites in the mesoporous samples. Moreover, Ag/CeO$_2$-M samples had much more intrinsic defect sites in fluorite structure than CeO$_2$-M. These results suggested that the loaded Ag species affected the content of oxygen vacancies in the mesoporous CeO$_2$. Evidently, Ag(2%)/CeO$_2$-M had the highest content of oxygen vacancies among the mesoporous samples.

The high-resolution XPS surface probe technique were used to investigate the surface composition and chemical state of different element in CeO$_2$-M, Ag(1%)/CeO$_2$-M, Ag(2%)/CeO$_2$-M, and Ag(3%)/CeO$_2$-M. The survey spectra indicated that Ce and O existed on the surface of CeO$_2$-M, and Ce, O, and Ag made up Ag/CeO$_2$-M (Fig. 4a). For all samples, the Ce 3d XPS spectrum could be separated into eight spectral components, which were attributed to v, v$_1$, v$_2$, v$_3$, u, u$_1$, u$_2$, and u$_3$, respectively (Fig. 4b). The peaks signed as v, v$_2$, and v$_3$ were ascribed to Ce^{4+} 3d$_{5/2}$, and the peaks signed as u, u$_2$, and u$_3$ were assigned to Ce^{4+} 3d$_{3/2}$. The v$_1$/u$_1$ doublet is assigned to the characteristic peak of Ce^{3+} 3d$_{5/2}$ and 3d$_{3/2}$, respectively. However, v$_1$/u$_1$ doublet was no found in the Ce 3d spectrum of CeO$_2$-B, indicating that almost no Ce^{3+} existed on the surface of CeO$_2$-B (Fig. S3a). The calculated surface concentration of Ce^{3+} for CeO$_2$-M, Ag(1%)/CeO$_2$-M, Ag(2%)/CeO$_2$-M, and Ag(3%)/CeO$_2$-M was 12.93, 18.56, 20.74, and 19.30%, respectively. Obviously, the Ce^{3+} concentration in Ag/CeO$_2$-M was higher than that of CeO$_2$-M, indicating that the introduction of Ag species into CeO$_2$ resulted in the partial reduction of Ce^{4+}. It can be found that Ag(2%)/CeO$_2$-M contained the most Ce^{3+}, and namely the highest content of oxygen vacancies, which possibly promote the photocatalytic disinfection by activating reactants [25]. According to Fig. 4c and Fig. S3b, the O 1s peak of all the samples could be separated into three component peaks. The first one at the lowest binding energy was attributed to lattice oxygen (O^{2-}), the second peak at the middle binding energy was ascribed to chemisorbed oxygen species (O$_2^{2-}$), and the third peak with the highest binding energy was due to surface hydroxyl species or adsorbed water on the surface of CeO$_2$ (OC) [25,31]. The ratio of chemisorbed oxygen species for CeO$_2$-B, CeO$_2$-M, Ag(1%)/CeO$_2$-M, Ag(2%)/CeO$_2$-M, and Ag(3%)/CeO$_2$-M was 36.11%, 36.28%, 39.36%, 44.01%, and 43.00%, respectively. It could be found that CeO$_2$-M had a little more chemisorbed oxygen species than CeO$_2$-B. In other words, the introduction of Ag species could give rise to more chemisorbed oxygen species on the surface of Ag/CeO$_2$-M samples, and the highest one was observed for Ag(2%)/CeO$_2$-M. In the Ag 3d spectrum of Ag/CeO$_2$-M (Fig. 4d), the two peaks around 374.5 eV and

368.5 eV were assigned to Ag 3d$_{3/2}$ and Ag 3d$_{5/2}$, respectively, with the spin energy separation of 6.0 eV corresponding to metallic silver Ag [37].

3.2. Photocatalytic disinfection performance

The disinfection effect of as-prepared samples (CeO$_2$-B, CeO$_2$-M, Ag(1%)/CeO$_2$-M, Ag(2%)/CeO$_2$-M, and Ag(3%)/CeO$_2$-M) was investigated by using *E. coli* as the model bacterium. The CeO$_2$-B and CeO$_2$-M samples showed negligible disinfection efficiencies in the dark, indicating their low cytotoxicity to *E. coli* without the irradiation of visible light (Fig. 5a). Ag/CeO$_2$ composites exhibited little disinfection efficiencies, with the highest value of 1.11 log inactivation *E. coli* for Ag(3%)/CeO$_2$ composites, possibly ascribing to the deposited Ag species, which was considered as a common antibacterial material [5]. As shown in Fig. 5b, almost no *E. coli* was inactivated in the absence of photocatalysts under visible light illumination (light control). The CeO$_2$-B exhibited very low bactericidal efficiency with only about 0.87 log inactivation of *E. coli* cells after 150 min of visible light exposure. As for CeO$_2$-M, the inactivation efficiency was higher than CeO$_2$-B, with 1.86 log inactivation of *E. coli*. In contrast to CeO$_2$-B and CeO$_2$-M, the bactericidal efficiency of Ag/CeO$_2$-M enhanced greatly with Ag doping. Particularly, over 150 min of visible light exposure, the amount of viable bacteria is $10^{2.35}$, 0, and $10^{1.65}$ for Ag(1%)/CeO$_2$-M, Ag(2%)/CeO$_2$-M, and Ag(3%)/CeO$_2$-M, respectively. For comparison, the bactericidal effect of Ag(1%)/CeO$_2$-B, Ag(2%)/CeO$_2$-B, and Ag(3%)/CeO$_2$-B was shown in Fig. S5. The amount of viable bacteria is $10^{5.90}$, $10^{5.01}$, and $10^{5.70}$ for Ag(1%)/CeO$_2$-B, Ag(2%)/CeO$_2$-B, and Ag(3%)/CeO$_2$-B after 150 min of irradiation, respectively. It can be found that Ag/CeO$_2$-M presented much better disinfection effect than the corresponding Ag/CeO$_2$-B samples. Ag(2%)/CeO$_2$-M displayed the best disinfection efficiency despite its moderate Ag content. According to the XPS results, Ag(2%)/CeO$_2$-M had the highest concentrations of oxygen vacancies and the chemisorbed oxygen species among all the prepared photocatalysts, which could explain its best disinfection efficiency. Since oxygen vacancies could promote the formation of superoxide species by providing active sites, more oxygen vacancies could be favorable to the photocatalytic process. It also has been reported that oxygen vacancies could improve the photocatalytic efficiency by accelerating the separation of photogenerated electron-hole pairs [22]. Additionally, in order to further verify the enhanced photocatalytic activity of Ag/CeO$_2$-M,
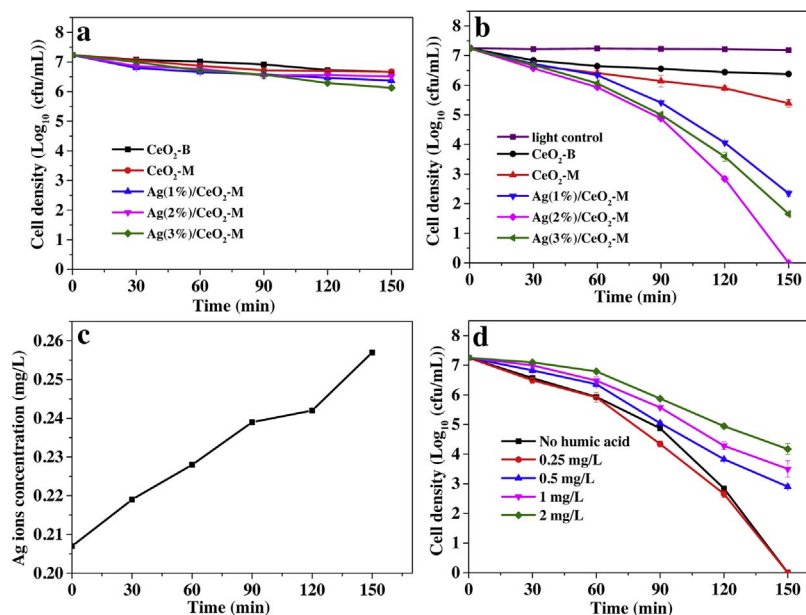
Fig. 5. (a) Inactivation efficiency against *E. coli* (10^7 cfu/mL) with tested samples (100 μg/mL) in the dark, (b) photocatalytic inactivation efficiency against *E. coli* (10^7 cfu/mL) with tested samples (100 μg/mL) under visible light irradiation, (c) Ag ions leaking from Ag(2%)/CeO_2-M (100 μg/mL) in 0.85% NaCl solution with *E. coli* cells (10^7 cfu/mL) under visible light irradiation, and (d) effect of humic acid concentrations on the photocatalytic inactivation efficiency toward *E. coli* (10^7 cfu/mL) in the presence of Ag (2%)/CeO_2-M (100 μg/mL).

tartrazine, a common organic dye, was selected as a target pollutant. As shown in Fig. S6, CeO_2-M showed better degradation efficiency than CeO_2-B, and the efficiency of CeO_2-M greatly improved after Ag doped. For Ag/CeO_2-M samples, the degradation efficiency of tartrazine exhibited the similar tendency as *E. coli* with Ag(2%)/CeO_2-M showing the best photocatalytic activity. In a word, the Ag/CeO_2-M composite obtained excellent degradation effect towards different pollutants, which indicated its versatility and potential in treating practical wastewater with complicated components.

The PL spectra of CeO_2-M, Ag(1%)/CeO_2-M, Ag(2%)/CeO_2-M, and Ag(3%)/CeO_2-M were conducted to examine the recombination of electron-hole pairs in the prepared mesoporous samples. The PL spectra at the excitation wavelength of 364 nm were shown in Fig. S7. It could be found that the emission peaks of all samples had the similar shape and centered at about 490 nm. The emission peak intensities of the Ag/CeO_2-M composites were weaker than that of CeO_2-M, indicating that the introduction of Ag species can effectively suppress the recombination of electron and hole pairs. Ag nanoparticles could act as electron sinks, efficiently trapped photogenerated electrons and hampered the recombination of free charge carriers. It was found that the Ag(2%)/CeO_2-M displayed the lowest emission peak, indicating the lowest recombination of free charge carriers. This results could be responsible for the best of disinfection effect of Ag(2%)/CeO_2-M. The heterogeneous interface between Ag and CeO_2-M nanoparticles played an important role in the photo-activity, since excess Ag species in Ag(3%)/CeO_2-M possibly act as recombination centers, instead of enhancing charge separation. The PL spectra results were also consistent with the concentrations of oxygen vacancies and chemisorbed oxygen species, among which Ag(2%)/CeO_2-M had the highest values.

It was quite possible that there were some Ag ions leaked during the photocatalytic process because of the high oxidative power of in-situ formed h^+ and other reactive species. To investigate the contribution of Ag^+ to the disinfection effect, we measured the leakage of Ag ion from Ag(2%)/CeO_2-M during the photocatalytic process. In Fig. 5c, the Ag ions concentrations increased gradually with the extension of disinfection time which was below 0.3 mg/L at end of the disinfection. This dose had little bactericidal effect (about l log inactivation effect) under the same experimental condition (Fig. S8). Therefore, Ag^+ had little contribution to the excellent disinfection effect of Ag(2%)/CeO_2-M. The leakage of Ag^+ is popular for the Ag-containing nanomaterials when applied in water disinfection. Xia et al. reported the inactivation mechanisms of bacteria by graphene sheets grafted plasmonic Ag-AgX

photocatalyst, and 0.58 mg/L Ag^+ was detected at the end of the disinfection process [11]. Xiao et al. reported the photocatalytic antimicrobial effects and mechanism of Ag-nanoparticles@chitosan-TiO_2 composites for water disinfection, and the composites exhibited about 1 mg/L of Ag^+ leakage after 180 min of irradiation [44]. Zhang et al. reported the photocatalytic bactericidal effect of *E. coli* K12 using AgBr-Ag-Bi_2WO_6 composite under visible light, and 0.55 mg/L Ag^+ was detected in suspension of the materials and bacteria [45]. However, in our work, the Ag^+ concentration is below 0.3 mg/L at end of the disinfection, which is much smaller than these above reported values.

3.3. The influence of humic acid

Humic acid (HA) is the main constituent of natural organic matter and widely exists in the environment. It belongs to a chemically heterogeneous compound including abundant functional groups such as amine, hydroxyl, and carboxyl. HA plays an important role in the photochemical processes in waters. In this work, the influence of HA with different concentrations on the disinfection efficiency was investigated. As shown in Fig. 5d, HA concentration-dependent decline in disinfection effect was observed. Remarkably, in the presence of 0.25 mg/L HA, the disinfection efficiency was increased compared to the control (treatment without addition of HA). With the further increase of HA concentrations to 0.5, 1 and 2 mg/L, the disinfection efficiency was decreased dramatically compared to these of 0.25 mg/L and control treatment. It has been reported that humic acid substances containing large amounts of chromophores can be sensitized by sunlight resulting in formation of triplet excited states ^{3}DOM*, which can further react with O_2 through a serious of energy or electron transfer processes to produce reactive oxygen species such as ·OH, H_2O_2 [46]. However, high concentration of humic acid in water could have adverse effect on the photocatalytic activity because the degradation of humic acid substances themselves competed with the object pollutants for reactive species [37]. In addition, HA could provide *E. coli* with protective effect against adverse illumination by absorbing light over wavelengths from 270 to 500 nm [47].

3.4. Detection of ·OH and ·O_2^- by ESR

The ESR spectra of CeO_2-B, CeO_2-M, Ag(1%)/CeO_2-M, Ag(2%)/CeO_2-M, and Ag(3%)/CeO_2-M were measured using DMPO as radical trapper under visible light illumination to detect ·OH and ·O_2^- in the
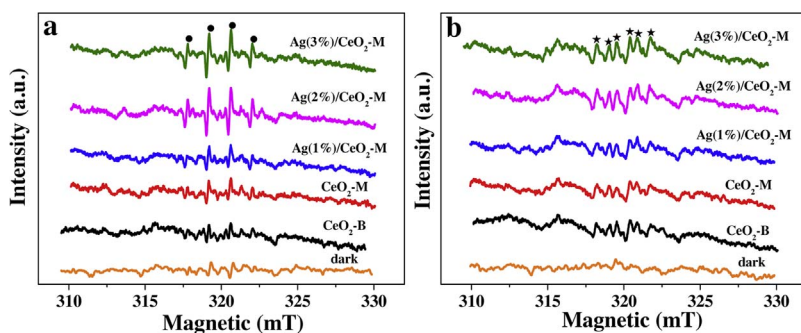
Fig. 6. ESR spectra of all the photocatalysts in H_2O (a) and CH_3OH (b) solvent with DMPO as the radical trapper.

reaction system. No signals could be detected for both ·OH and ·O_2^- in the dark (Fig. 6). Under the visible light exposure, the quadruple peaks with intensity 1:2:2:1 of the DMPO-·OH adducts could be observed as labeled by the circles. In addition, the sextet peaks of the DMPO-·O_2^- adducts were also observed as indicated by the pentagram. It can be found that Ag(2%)/CeO_2-M had the strongest peaks intensity both for ·OH and ·O_2^-. The intensity of ·OH and ·O_2^- in the ESR was well consistent with the result of disinfection efficiency in Fig. 5b.

3.5. Oxidative stress induced by Ag(2%)/CeO₂-M

Generally speaking, SOD and CAT are well-known antioxidant enzymes that protect bacteria from oxidative stress. They can be regarded as effective indicators of oxidative stress in bacterial cell suffering adverse situations such as UV irradiation. The irradiation induced SOD and CAT activities are shown in Fig. 7a and b. The activity of SOD and CAT exhibited the similar tendency that their levels increased greatly within the first 15 min and reached the maximum values. These observations suggested that a mass of SOD and CAT were produced in the initial phase of the disinfection process which were the inherent defense behaviors of bacteria protecting them from the attack of active oxidative species such as ·O_2^- and H_2O_2. Thereafter, the activity of SOD and CAT decreased as the bactericidal efficiency increased, implying the amount of reactive oxidative species produced by Ag(2%)/CeO_2-M exceeded the self-defense capability of *E. coli*.

3.6. Cell integrity destruction

Two fluorescent nucleic acid dyes, SYTO9 and PI, were used to stain DNA of *E. coli*. SYTO9 is a cell-permeable, green fluorescent stain for both live and dead bacteria, and PI is a cell-impermeable, red fluorescent stain for cells with compromised cellular membranes. As shown in Fig. 8, there were almost no dead cells at 0 min. After 30 min of irradiation, some of the cells displayed red fluorescence, indicating that the integrities of these cells had been destroyed. After 60 min of irradiation, most of *E. coli* cells were adsorbed on Ag(2%)/CeO_2-M and exhibited red fluorescence after PI staining; however, a large proportion of the cells in the free state were still alive. As the irradiation time was extended to 90 min, most of the bacteria were absorbed on the Ag(2%)/

CeO_2-M surface and had died because of the direct attack of the biocidal reactive species on the surface. Many of the free bacteria had also been killed, indicating that some reactive species with long lifetimes could diffuse into the bulk solution and destroy the cell bodies. At the end of the exposure, all of the bacteria cells, whether in the absorbed or free state, were killed by reactive species generated by Ag(2%)/CeO_2-M.

The morphology of *E. coli* at different stages of the disinfection process was imaged by SEM and AFM. At the beginning of exposure (Fig. 9a), the *E. coli* cells presented intact cell membranes and standard rod-shaped morphology with lengths of approximately 1–2 μm. Moreover, the start of the cell division process could be observed, as indicated by the green arrow in Fig. 9a. After 30 min of exposure, the cell bodies were deformed, and their surfaces were wrinkled with small bulges and pits (Fig. 9b), indicating that reactive species had been generated on the surface of Ag(2%)/CeO_2-M under excitation by visible light and that these species had begun to destroy the outer wall and membrane of *E. coli*. As shown in Fig. 9c, after 60 min of exposure, the shapes of the cells were further distorted, and large holes appeared on their surface because of the attack of the reactive species. With the extension of exposure to 90 min (Fig. 9d), the cells became seriously misshapen, and their membranes became extensively fractured, which caused leakage of the internal cell contents. Most of the cell bodies were absorbed and gathered together on the Ag(2%)/CeO_2-M surface, which restricted the free activity of *E. coli*. The *E. coli* cells were completely deformed after 120 min of exposure, as indicated by the green ellipse in Fig. 9e. The cell residue was combined with the Ag(2%)/CeO_2-M biocide, which promoted the degradation of intracellular components by reactive species, and it was difficult to distinguish the pristine morphology of *E. coli*. As shown in Fig. 9f–j, AFM images also revealed the time-dependent morphology changes of *E. coli* cells. It was worth noting that large amounts of linear and round substances appeared at the end of disinfection (Fig. 9j). These substances were supposed to be the cell inclusions or their residues after degradation.

3.7. DFT calculation

The mutual interaction between Ag and mesoporous CeO_2 support was further theoretically investigated by DFT calculations (all CeO_2 in this part represent mesoporous CeO_2). According to the HRTEM image
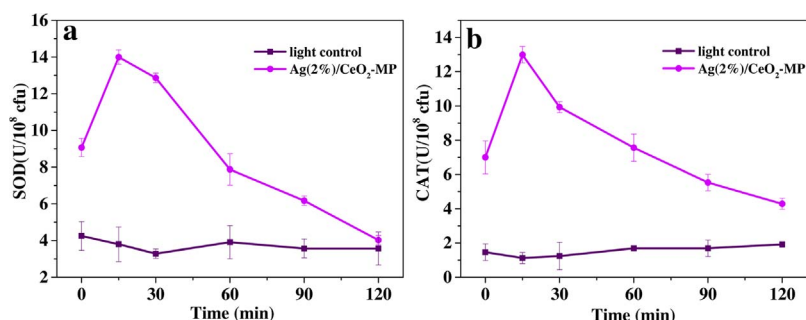

Fig. 7. SOD (a) and CAT (b) activities during the photocatalytic disinfection process against *E. coli* (10^8 cfu/mL).
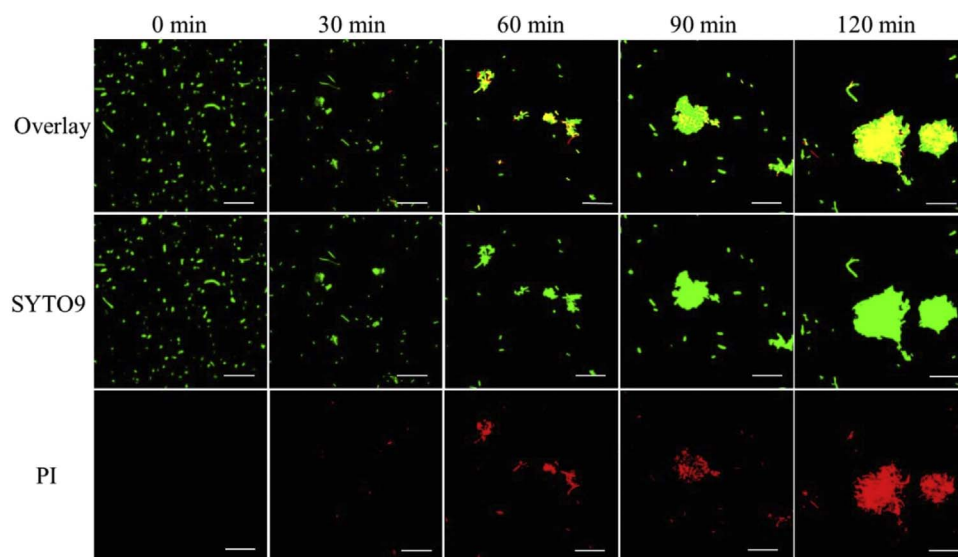
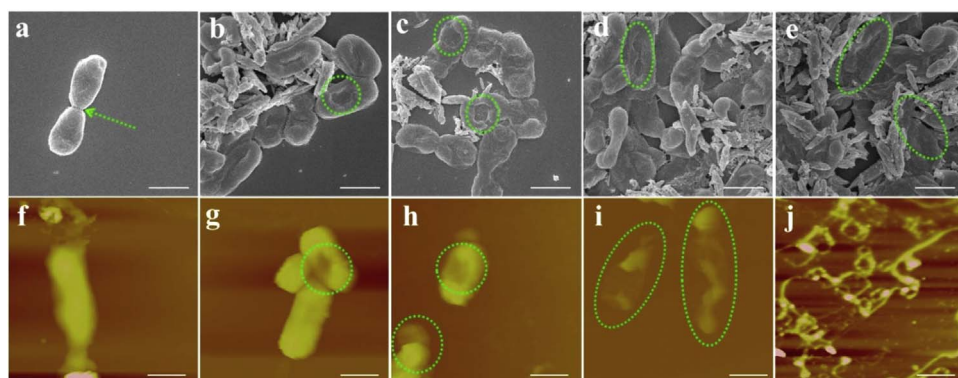**Fig. 8.** Confocal fluorescent images of live and dead *E. coli* (10^9 cfu/mL), the scale bar is 20 µm.

Fig. 9. SEM (a–e) and AFM (f-j) images of *E. coli* treated with Ag(2%)/CeO$_2$-M (100 µg/mL) under visible light: (a, f) 0 min, (b, g) 30 min, (c, h) 60 min, (d, i) 90 min, (e, j) 120 min. The green circle and ellipse indicate the deformation, pore-forming and fracture of *E. coli*. The scale bar is 1 µm. (For interpretation of the references to colour in this figure legend, the reader is referred to the web version of this article.)

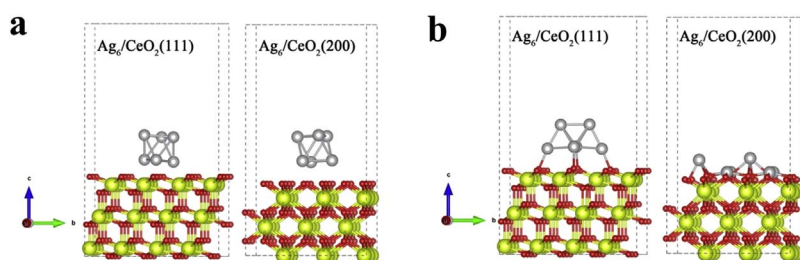**Fig. 10.** Adsorption models to simulate the mutual interaction between Ag$_6$ cluster and CeO$_2$-(111) and CeO$_2$-(200) surfaces, (a) the initial constructed structures and (b) the optimized adsorption geometries. The balls in yellow, red and gray represent Ce, O and Ag atoms, respectively. (For interpretation of the references to colour in this figure legend, the reader is referred to the web version of this article.)

in Fig. 1f, the main exposed planes of CeO$_2$ were ascribed to {111} crystal families along with a few belonged to {200} crystal families. Therefore, slabs models with both (111) and (200) as exposed plane were constructed to simulate the CeO$_2$ support, and Ag$_6$ cluster was placed on the slabs to form Ag$_6$/CeO$_2$-(111) or Ag$_6$/CeO$_2$-(200) composites, respectively (Fig. S9 and 10a). These slabs were used as initial configurations for structural optimization, and Ag-CeO$_2$ composite models were constructed on the basis of optimized slabs as shown in Fig. 10b. The adhesion energy of Ag cluster on CeO$_2$ (111) or (200) surface was calculated according to the following equations:

$$Ead111 = EAg/CeO2\text{-}111 - ECeO2\text{-}111 - EAg \quad (2)$$

$$Ead200 = EAg/CeO2\text{-}200 - ECeO2\text{-}200 - EAg \quad (3)$$

Where $E_{Ag/CeO2}$, E_{CeO2} and E_{Ag} represents the total energies of interacting Ag-CeO$_2$ system, CeO$_2$ surface slabs and Ag cluster, respectively.

Among the low-indexed surfaces of stoichiometric cerium oxide, both DFT calculation and experimental observation confirmed the (111) was the most stable plane [48]. Herein, during the optimization of slab models of CeO$_2$-(111) and CeO$_2$-(200) surfaces, a very big magnetization (mag. = 12.51 A/m) was found in CeO$_2$-(200) surface, which indicated amount of unoccupied single paramagnetism electrons existed and would cause the rise of surface energy. Besides, the calculated adsorption energy for CeO$_2$-(111) and CeO$_2$-(200) surfaces was -0.494 eV/f.u. and -2.752 eV/f.u., respectively. The negative value of adhesion energies illustrated the mutual interaction between Ag$_6$ cluster and CeO$_2$-(111) or CeO$_2$-(200) surface was thermodynamic favor process, which leads to a stabilizing interaction. Moreover, the more negative value of adhesion energy for CeO$_2$-(200) surfaces also illustrated its less stable. Therefore, {111} crystal family was considered to be the main exposed plane in as-synthesized mesoporous CeO$_2$ nanostructure and only Ag$_6$/CeO$_2$-(111) composite was considered for further electronic structure analysis.

To further understand the electronic structure changes and charge redistribution after Ag$_6$ cluster loaded, the density of state (DOS) and charge density analysis were done for Ag$_6$ cluster, clean CeO$_2$-(111) and
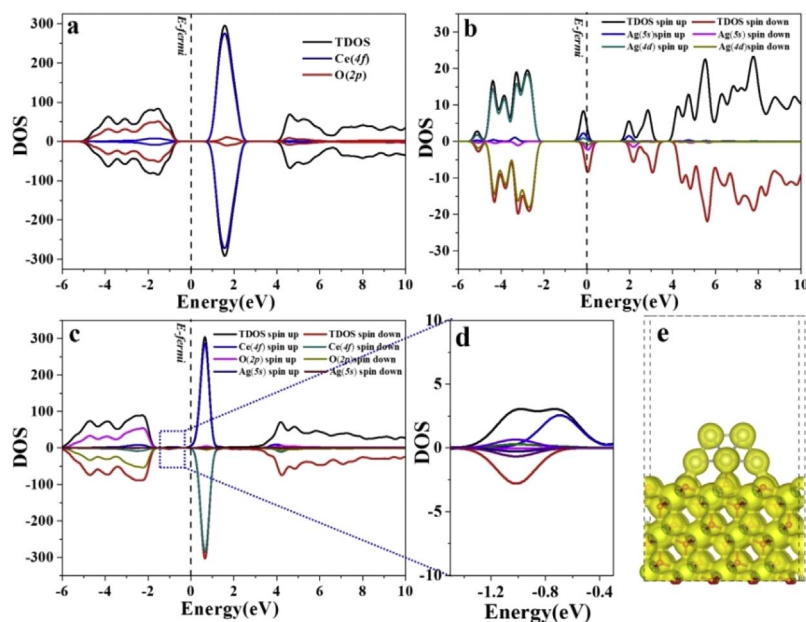
Fig. 11. Density of state of CeO₂-111 surface (a), Ag₆ cluster (b) and Ag₆/CeO₂-(111) composite (c), the enlarged image of midgap states (d), charge density distribution with isosurface level set at $0.05a_0^{-3}$, where a_0 is the Bohr radius (e).

Ag₆/CeO₂-(111) composite. As shown in Fig. 11a, the valence band edge in CeO₂ was primarily derived from O2p orbitals while the conduct band edge from Ce4f orbitals. For Ag₆ cluster, the Fermi level traversed Ag5 s orbitals which also revealed its metal nature (Fig. 11b). For the Ag₆/CeO₂-(111) composite, midgap states above the valence band of CeO₂ were generated from the hybridization of O2p and Ag5 s orbitals (Fig. 11c and d). The midgap states can accommodate the electrons photogenerated from the valence band of Ag₆/CeO₂-(111) composite, significantly lowering the threshold of incident photon energy and broaden the adsorption spectrum. In addition, it has been reported that the midgap states could serve as the separation centers to trap the photoinduced electrons and suppress the charge recombination [49]. To give an intuitive image of the mutual interaction, charge density distribution was calculated as shown in Fig. 11e, and the electron density overlap between Ag and O atoms on the surface illustrated hybridization of O2p and Ag5 s orbitals which was consistent with above DOS analysis.

3.8. The mechanism of enhanced photocatalytic inactivation by Ag(2%)/CeO₂-M

The photocurrents generated from CeO₂-M and Ag(2%)/CeO₂-M were surveyed under visible light with several on-off cycles. As shown in Fig. S10a, comparing to CeO₂-M, the photocurrent response of the Ag(2%)/CeO₂-M was significantly increased under visible light irradiation. The increased photocurrent of Ag(2%)/CeO₂-M could be ascribed to the efficient electron transfer from the conduction band of CeO₂-M to Ag nanoparticles as efficient electron sinker. Moreover, Ag(2%)/CeO₂-M contained more oxygen vacancies than CeO₂-M, which could facilitate the separation of photogenerated electron-hole pairs. The enhanced photocurrent from Ag(2%)/CeO₂-M suggested faster separation of the photogenerated electron-hole pairs and longer lifetime of the free charge carriers compared to CeO₂-M, which was consistent with the better disinfection efficiency of Ag(2%)/CeO₂-M. Furthermore, the arc radius on the EIS plots of Ag(2%)/CeO₂-M was smaller than that of CeO₂-M under visible light (Fig. S10b), indicating that the separation and transport efficiency of photogenerated electron and hole pairs was significantly enhanced after the introduction of Ag species.

With Ag species doping, the absorptions in visible light region were increased greatly and the absorption edges shifted toward high wavelength (Fig. 12a). This stronger visible light response may be attributed to the SPR effect of Ag nanoparticles and the enhancement of oxygen

vacancies by Ag species in the CeO₂-M [31]. The band gap energies of CeO₂-M and Ag(2%)/CeO₂-M was 2.70 and 2.51 eV, respectively (Fig. 12b). According to Mott-Schottky (MS) plots in Fig. 12c, the flat band potential of CeO₂-M and Ag(2%)/CeO₂-M is −0.76 V and −0.3 V, respectively, which is close to the conduction band edge. Thus, the valence band edge of CeO₂-M and Ag(2%)/CeO₂-M could be estimated to be 1.94 and 2.21 V, respectively. This result indicated that the valence band edge of Ag(2%)/CeO₂-M was lowered than that of CeO₂-M by 0.30 V. Theoretically, Ag(2%)/CeO₂-M, with lower valence band edge, produces holes with stronger oxidation ability, resulting in better disinfection efficiency.

The reactive species including h⁺, ·OH and e⁻ are usually considered to be the determining factors for the photocatalytic disinfection activity [50]. The concentrations of the reactive species were evaluated by adding specific chemical scavengers. The results indicated that the h⁺ was the most abundant active species, following was e⁻, and the least is ·OH during the photocatalytic inactivation process (Fig. 12d). Therefore, the possible enhanced disinfection mechanism of Ag(2%)/CeO₂-M was proposed in Fig. 13. Firstly, water, O₂, and *E. coli* were adsorbed on the surface of Ag(2%)/CeO₂-M samples. Secondly, the electrons on valence band (VB) transferred to the conduction band (CB) leaving hole (h⁺) with higher oxidation power on valence band under visible light. The free e⁻ on the conduction band could be trapped by Ag species which could inhibit the recombination of h⁺ and e⁻. The e⁻ could transform into ·O₂⁻ and ·OH with oxidative power. Since all the above processes are closely related to the intrinsic properties of a photocatalyst, including textural, surface, crystal, and electronic structures, an effective approach integrating the above properties could optimize, coordinate these processes, and further obtain a significant enhancement of the photocatalytic disinfection effect [51]. In this work, the mesoporous structure can not only promote the light harvesting by enhancing the optical path through the multiple scattering effect, but also provide bigger surface area facilitating the adsorption and transportation of reactants and products [31]. The SPR effect of Ag nanoparticles was conducive to visible light harvesting and Ag nanoparticles could be as effective electron sinkers [37]. The Ag(2%)/CeO₂-M had high surface chemisorbed oxygen species which could trap free electrons and yield surface oxygen species. Additionally, the high percentage of Ce³⁺ on the surface of Ag(2%)/CeO₂-M indicated that the partial metal in composites was not fully oxidized, and thus Ce³⁺ can interact with holes and inhibit the recombination of electrons and holes [30]. On the one hand, the midgap states induced by Ag doping could
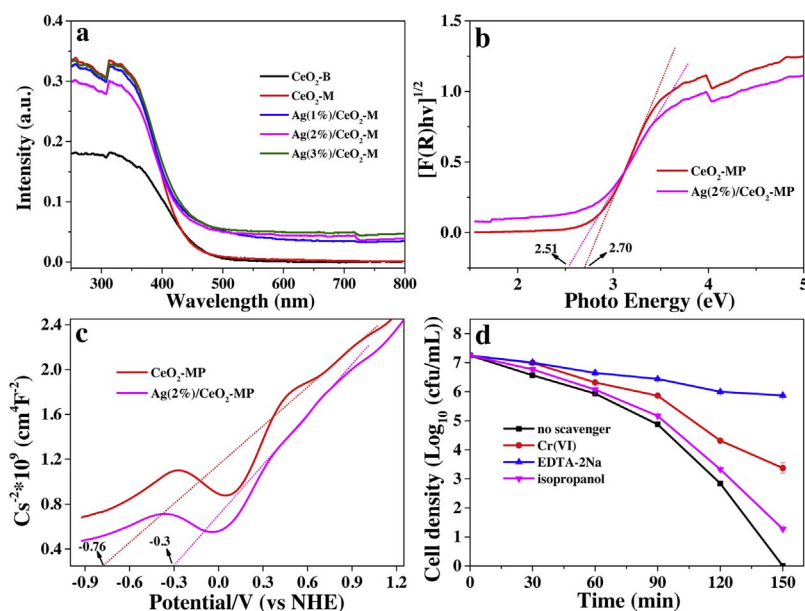
Fig. 12. (a) UV-vis/DRS, (b) plot of $[F(R)h\nu]^{1/2}$ vs. photon energy (eV), (c) Mott-Schottky (MS) plots, and (d) photocatalytic inactivation efficiency against *E. coli* (10^{7} cfu/mL) in the presence of Ag(2%)/CeO$_2$-M (100 µg/mL) with different scavengers (0.02 mmol/L Cr(VI), 0.5 mmol/L isopropanol, 0.1 mmol/L EDTA-2Na) under visible light.
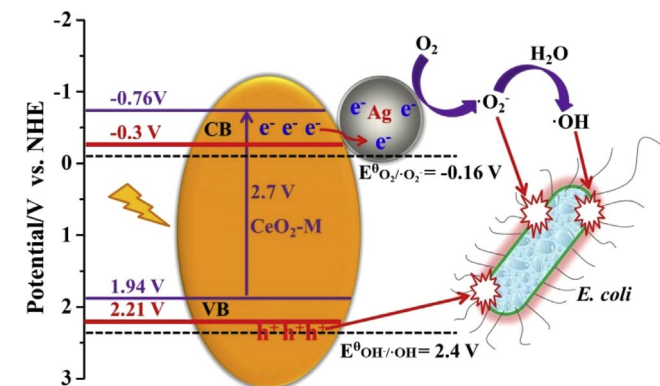

Fig. 13. The mechanism of *E. coli* disinfection with Ag(2%)/CeO$_2$-M under visible light.

extend the adsorption edge toward high wavelength by enhancing the absorption of photons with energies smaller than the band gap [52]. The midgap states could also act as trappers to capture photo-excited electrons and therefore accelerate the separation of electron-hole pairs [49]. The valence band edge of Ag(2%)/CeO$_2$-M was downshifted by 0.30 V compared with that of CeO$_2$-M, suggesting higher oxidative power of hole in the former. Since the Ag(2%)/CeO$_2$-M has integrated the ordered mesoporous structure, high content of surface oxygen vacancy, the SPR effect of Ag, the midgap states and high oxidative power of hole together, a strong synergetic enhancement in the photocatalytic disinfection is achieved.

4. Conclusions

In this work, highly ordered mesoporous Ag/CeO$_2$ nanocomposites were prepared by photo-assisted reduction of silver on mesoporous CeO$_2$, which was synthesized using the nanocasting technique. Doping Ag species could extend the absorption range to visible light area and enhance the concentration of Ce^{3+} ions and oxygen vacancies. It was found that these mesoporous Ag/CeO$_2$ nanocomposites exhibited superior photocatalytic disinfection efficiency for the inactivation of *E. coli* compared with mesoporous CeO$_2$ and bulk CeO$_2$, respectively. The enhanced disinfection mechanism was attributed to the fact that the novel mesoporous structure can promote the mass-transfer process and the interfacial interaction between Ag species and CeO$_2$ lead to reduced recombination of free charges, rapid separation and transportation of photogenerated electrons-holes. In a word, this work paves a novel approach to design mesoporous plasmonic photocatalysts for pathogenic bacteria inactivation using the abundant solar radiation.

Appendix A. Supplementary data

Supplementary data associated with this article can be found, in the online version, at http://dx.doi.org/10.1016/j.apcatb.2017.10.032.

References

[1] C. Martinez-Huitle, E. Brillas, Angew. Chem. Int. Ed. 47 (2008) 1998–2005.
[2] V.K. Sharma, N. Johnson, L. Cizmas, T.J. Mcdonald, H. Kim, Chemosphere 150 (2016) 702–714.
[3] J. Zhang, Z. Wei, H.F. Jia, X. Huang, Front. Environ. Sci. Eng. 11 (2017) 8.
[4] A.K. Epstein, B. Pokroy, A. Seminara, J. Aizenberg, Proc. Natl. Acad. Sci. U. S. A. 108 (2011) 995–1000.
[5] S.L. Ma, S.H. Zhan, Y.N. Jia, Q.X. Zhou, ACS Appl. Mater. Interfaces 7 (2015) 10576–10586.
[6] O.K. Dalrymple, E. Stefanakos, M.A. Trotz, D.Y. Goswami, Appl. Catal. B 98 (2010) 27–38.
[7] X.F. Yang, J.L. Qin, Y. Jiang, K.M. Chen, X.H. Yan, D. Zhang, Appl. Catal. B 166-167 (2015) 231–240.
[8] X.F. Yang, J.L. Qin, Y. Jiang, R. Li, Y. Li, H. Tang, RSC Adv. 4 (2014) 18627–18636.
[9] S.L. Ma, S.H. Zhan, Y.N. Jia, Q.X. Zhou, ACS Appl. Mater. Interfaces 7 (2015) 21875–21883.
[10] C. George, A. Beeldens, F. Barmpas, J.-F. Doussin, G. Manganelli, H. Herrmann, J. Kleffmann, A. Mellouki, Front. Environ. Sci. Eng. 10 (2016) 2.
[11] D.H. Xia, T.C. An, G.Y. Li, W.J. Wang, H.J. Zhao, P.K. Wong, Water Res. 99 (2016) 149–161.
[12] S.C. DeCaluwe, M.E. Grass, C. Zhang, F.E. Gabaly, H. Bluhm, Z. Liu, G.S. Jackson, A.H. McDaniel, K.F. McCarty, R.L. Farrow, J. Phys. Chem. C 114 (2010) 19853–19861.
[13] X. Wang, N.S.J. Gao, Q.X. Zhou, Biosen. Bioelectron. 43 (2013) 264–267.
[14] R. Suresh, V. Ponnuswamy, R. Mariappan, Ceram. Int. 40 (2014) 13515–13527.
[15] T. Naganuma, E. Traversa, Biomaterials 35 (2014) 4441–4453.
[16] A. Corma, P. Atienzar, H. Garcia, J. Chane-Ching, Nat. Mater. 3 (2004) 394–397.

[17] X.J. Wen, C.G. Niu, M. Ruan, L. Zhang, G.M. Zeng, J. Colloid Interface Sci. 497 (2017) 368–377.
[18] X.J. Wen, C.G. Niu, L. Zhang, G.M. Zeng, Dalton Trans. 46 (2017) 4982–4993.
[19] X.J. Wen, C. Zhang, C.G. Niu, L. Zhang, G.M. Zeng, X.G. Zhang, Catal. Commun. 90 (2017) 51–55.
[20] Y.G. Wang, F. Wang, Y.T. Chen, D.F. Zhang, B. Li, S.F. Kang, X. Li, Appl. Catal. B 147 (2014) 602–609.
[21] Q.X. Zhou, Y. Cheng, Q.R. Zhang, J.D. Liang, Sci. China Life Sci. 47 (2004) 332–339.
[22] Y.C. Huang, B. Long, M.N. Tang, Z.B. Rui, M. Balogun, Y.X. Tong, H.B. Ji, Appl. Catal. B 181 (2016) 779–787.
[23] C.E. Castano, M.J. O'Keefe, W.G. Fahrenholtz, Curr. Opin. Solid State Mater. Sci. 19 (2015) 69–76.
[24] B.Y. Bai, J.H. Li, J.M. Hao, Appl. Catal. B 164 (2015) 241–250.
[25] D. Jiang, W.Z. Wang, L. Zhang, Y.L. Zheng, Z. Wang, ACS Catal. 5 (2015) 4851–4858.
[26] D.S. Zhang, H.X. Fu, L.Y. Shi, J.H. Fang, Q. Li, J. Solid State Chem. 180 (2007) 654–660.
[27] J. Li, A. Kalam, A.S. Al-Shihri, Q.M. Su, G. Zhong, G.H. Du, Mater. Chem. Phys. 130 (2013) 1066–1071.
[28] Q.G. Dai, S.X. Bai, H. Li, W. Liu, X.Y. Wang, G.Z. Lu, CrystEngComm 16 (2014) 9817–9827.
[29] Y. Wang, D.Y. Zhao, Chem. Rev. 107 (2007) 2821–2860.
[30] Y.G. Wang, B. Li, C.L. Zhang, L.F. Cui, S.F. Kang, X. Li, L.H. Zhou, Appl. Catal. B 130-131 (2013) 277–284.
[31] Z.P. Qu, F.L. Yu, X.D. Zhang, Y. Wang, J.S. Gao, J. Chem Eng, 229 (2013) 522–532.
[32] M.Y. Mao, H.Q. Ly, Y.Z. Li, Y. Yang, M. Zeng, N. Li, X.J. Zhao, ACS Catal. 6 (2016) 418–427.
[33] B.W. Lu, K. Kawamoto, Mater. Res. Bull. 53 (2014) 70–78.
[34] S.J. Chang, M. Li, Q. Hua, L.J. Zhang, Y.S. Ma, B.J. Ye, W.X. Huang, J. Catal. 293 (2012) 195–204.
[35] A. Nakajima, T. Kobayashi, T. Isobe, S. Matsushita, Mater. Lett. 65 (2011) 3051–3054.
[36] N. Zhang, X.Z. Fu, Y.J. Xu, J. Mater. Chem. 21 (2011) 8152–8158.
[37] S.L. Ma, S.H. Zhan, Y.N. Jia, S. Qiang, Q.X. Zhou, Appl. Catal. B 186 (2016) 77–87.
[38] L.E. Wu, S.M. Fang, L. Ge, C.C. Han, P. Qiu, Y.J. Xin, J. Hazard. Mater. 300 (2015) 93–103.
[39] L. Ma, D.S. Wang, J.H. Li, B.Y. Bai, L.X. Fu, Y.D. Li, Appl. Catal. B 148-149 (2014) 36–43.
[40] X.G. Meng, L.Q. Liu, S.X. Ouyang, H. Xu, D.F. Wang, N.Q. Zhao, J.H. Ye, Adv. Mater. 28 (2016) 6781–6803.
[41] K. Soni, B.S. Rana, A.K. Sinha, A. Bhaumik, M. Nandi, M. Kumar, G.M. Dhar, Appl. Catal. B 90 (2009) 55–63.
[42] P.F. Ji, J.L. Zhang, F. Chen, M. Anpo, J. Phys. Chem. C 112 (2008) 17809–17813.
[43] C. Ho, J.C. Yu, T. Kwong, A.C. Mak, S. Lai, Chem. Mater. 17 (2005) 4514–4522.
[44] G. Xiao, X. Zhang, W.Y. Zhang, S. Zhang, H.J. Su, T.W. Tan, Appl. Catal. B 170-171 (2015) 255–262.
[45] L.S. Zhang, K.H. Wong, H.Y. Yip, C. Hu, J.C. Yu, C.Y. Chan, P.K. Wong, Environ. Sci. Technol. 44 (2010) 1392–1398.
[46] Y. Lester, C.M. Sharpless, H. Mamane, K.G. Linden, Environ. Sci. Technol. 47 (2013) 11726–11733.
[47] A. Muela, J.M. Garcia-Bringas, I. Arana, I. Barcina, Microb. Ecol. 40 (2000) 336–344.
[48] Z.X. Yang, T.K. Woo, J. Chem. Phys. 120 (2004) 7741–7749.
[49] J.R. Ran, T.Y. Ma, G.P. Gao, X.W. Du, S.Z. Qiao, Energy Environ. Sci. 8 (2015) 3708–3717.
[50] W.J. Wang, T.W. Ng, W.K. Ho, J.H. Huang, S.J. Liang, T.C. An, G.Y. Li, J.C. Yu, P.K. Wong, Appl. Catal. B 129 (2013) 482–490.
[51] S.W. Liu, J.Q. Xia, J.G. Yu, ACS Appl. Mater. Interfaces 7 (2015) 8166–8175.
[52] R. Beranek, H. Kisch, Photochem. Photobiol. Sci. 7 (2008) 40–48.